ADVANCED INTELLIGENT SYSTEMS
Open Access
www.advintellsyst.com

Toward Robotic Sensing and Swimming in Granular Environments using Underactuated Appendages

*Shivam Chopra, Drago Vasile, Saurabh Jadhav, Michael T Tolley, and Nick Gravish**

Granular environments, such as sand, are one of the most challenging substrates for robots to move within due to large depth-dependent forces, unpredictable fluid/solid resistance forces, and limited sensing capabilities. An untethered robot is presented, inspired by biological diggers like sea turtles, which utilize underactuated appendages to enable propulsion and obstacle sensing in granular environments. To guide the robot's design, experiments are conducted on test appendages to identify the morphological and actuation parameters for forward thrust generation. Obstacle sensing is observed in granular media by measuring the increased force on the moving appendage caused by changes in the granular flow around it. These results are integrated into an untethered robot capable of subsurface locomotion in a controlled granular bed like natural, loosely packed sand. The robot achieves subsurface "swimming" at a speed of 1.2 mm s^{-1}, at a depth of 127 mm, faster than any other reported untethered robot at this depth, while also detecting obstacles during locomotion via force sensors embedded in the appendages. Finally, subsurface robot locomotion in natural sand at the beach is demonstrated, a feat no other robot has accomplished, showcasing how underactuated structures enable movement and sensing in granular environments with limited limb control.

1. Introduction

Deformable ground such as soil, sand, snow, and extraterrestrial regolith is one of the most common surface substrates with which mobile animals and robots have to contend.[1] Although a considerable amount of research has been devoted to swimming in water or flying in the air, only in the last 15 years has attention been focused on movement across or within deformable ground.[2–4] One of the most common examples of deformable ground is granular media (GM) such as sand. Recently, the study of robots capable of burrowing in GM has been of growing interest due to their wide range of potential applications, including 1) search-and-rescue and mining operations, 2) the study of biological organisms and the resiliency of soils, 3) the exploration of seabeds, underground, and extraterrestrial environments, and 4) the monitoring of contaminants.[5]

Robot locomotion in GM is a challenging task because robots moving through GM face many challenges such as 1) very large resistive forces due to frictional resistance between sand grains, 2) nonzero yield stresses that cause unpredictable solid/fluid transitions, and 3) extremely limited opportunities for sensing obstacles. These conditions impose challenging requirements for the design of an autonomous robot capable of subsurface locomotion in GM. For example, a robot at just 10 cm below the surface experiences resistive stress on the order of 10^4 Pa, requiring high-force actuation as well as minimization of the overall size of the robot. Furthermore, the high granular pressure and abrasive environment require the use of strong and robust materials for long-term operation. Finally, all moving components and the robot body must be tightly sealed so that sand grains cannot penetrate interfaces which would cause rapid degradation of mechanical components and subsequently failure.

Early efforts to create robots capable of subsurface locomotion in GM largely focused on two fundamental approaches: 1) robots that use peristaltic body expansion and elongation and 2) undulatory robots that use body bending to effectively "swim" in sand. Earthworm-like peristaltic actuation has been incorporated in many burrowing soft robots.[6–9] Peristaltic actuation takes place through cyclic body expansion and elongation, which enables control of friction forces between the robot and the surrounding material to achieve anchoring (high friction), and extending forward (low friction). However, peristaltic actuation for GM locomotion presents challenges for autonomous, untethered operation. Many of these robots are made of soft, elastic bodies, and use soft pneumatic actuators and thus need to be connected to a pump or a source of pressurized air. While it is feasible for soft robots to operate with onboard pumps, pneumatic actuation within GM presents a further challenge as the pump must be able to pull in the surrounding air which may be challenging at higher depths in GM and impossible in submerged GM.

Undulatory, "sand-swimming", robots move as a result of lateral body bending and propulsive swimming forces that are

S. Chopra, D. Vasile, S. Jadhav, M. T. Tolley, N. Gravish
Mechanical and Aerospace Engineering
University of California San Diego
9500 Gilman Drive, La Jolla, CA 92093, USA
E-mail: ngravish@eng.ucsd.edu

The ORCID identification number(s) for the author(s) of this article can be found under https://doi.org/10.1002/aisy.202200404.

DOI: 10.1002/aisy.202200404

generated as the body sweeps through the sand. This method of locomotion was inspired by the sandfish lizard which is capable of rapidly burrowing into the sand to escape predators.[3] The early studies of undulatory locomotion in GM led to foundational developments in the modeling of GM through the application of the resistive force theory (RFT),[10,11] which was originally developed for the locomotion of worms in viscous fluids.[12] Comprehensive experiments, numerical simulation, and RFT calculations enabled researchers to design and optimize a seven-link undulatory robot and study optimal swimming gaits in the sand.[13] Undulatory locomotion is a compelling method for movement in GM; however, previous robot experiments took place in shallow, low-density plastic beads, and thus the resistive forces were comparatively small. In natural GM like sand, the forces are substantially larger, and it is unclear if current actuators would be capable of generating motion.

More recent work has demonstrated several promising approaches for granular locomotion. Robots that "grow" by extending only at the tip have demonstrated impressive locomotion capabilities using either a plant-root-inspired everting skin[14,15] or a growing 3D printing filament extruder mechanism.[16] These methods drastically reduce the friction against the body since only the tip of the robot moves through GM. However these approaches necessarily are tethered, and their capability for maneuvering within GM can be limited. Robots that use the helical motion of an auger have also been recently developed[7,17] to self-drill through the sand. These robots show promise; however, current implementations have only been tested for locomotion on the surface of GM, rather than for subsurface locomotion.

Appendage-driven locomotion in GM has several advantages over other approaches as the sweep of the appendages: 1) has the potential to detect obstacles away from the body, 2) can generate large propulsive forces through a wide "stroke", and 3) permits steering through differential appendage motion to achieve differential thrust. Appendage-enabled locomotion has been widely studied for transportation in air, water, and on-ground surface which has informed the design of many successful robots with exceptional dynamic locomotion capabilities.[18–22] However, because of the lack of physical models for the interaction of appendages having underactuated bending modes, appendage-enabled locomotion in GM is not well studied.[23,24] Furthermore, using appendages for granular locomotion presents challenging design hurdles that must be overcome. Appendages must generate high force during the power stroke, and low force during the return stroke, requiring appendage reconfiguration through the locomotion cycle. However, it would be very challenging to fully actuate appendages for reconfiguration because of the high-force requirements in GM. One potential route for appendage-driven locomotion was demonstrated through appendages with anisotropic compliance that produce forward propulsion using symmetrical oscillation of the fins.[23] However, compliant appendages have a fundamental problem in GM: due to the frictional resistance of GM (i.e., nonzero yield stress), an elastic appendage can get "stuck" in a deformed configuration if the elastic restoring stress is below the yield stress.[25,26] Thus, a combination of appropriate appendage actuation angles and compliance properties is required to ensure appendages are capable of generating net forward propulsion.

Despite these challenges, locomotion through appendages presents a significant opportunity for sensing obstacles within the GM. Navigation and sensing in GM is a significant challenge because there are limited sensors that can be used to avoid obstacles. The high acoustic dissipation in GM limits acoustic localization methods, and the low-/no-light environment inhibits vision-based navigation. However, appendage locomotion has the potential to enable nearby obstacle sensing by detecting changes in the flow/force response of GM during locomotion. Previous work has shown how tactile sensing can be used with machine learning to detect the shape of obstacles buried in sand through contact forces.[27,28] This method has produced promising results in rice grains but sensing using this method was challenging in the sand as it relied on probe being in contact with the obstacle. Recent work has demonstrated that objects surrounded by GM can be detected by measuring the forces arising due to granular pressure around an obstacle.[29] However, it is unclear if such detection can be performed by a mobile robot with appendages that require movement over a large range through the GM.

This work presents a design of an easily deployable untethered robot, driven by two anisotropic underactuated appendages, which can sense obstacles in GM (**Figure 1**A and Movie S1, Supporting Information). The novelty of this work comes from the use of underactuated appendages for generating propulsive forces to move the robot forward as well as sensing obstacles around the robot for navigation and avoidance. The appendages move in a sweep and propel motion generating asymmetric thrust by displacing the sand to swim in the grains. This work makes the following contributions in swimming and sensing in granular environments that form the basis of our robot design: 1) design of underactuated appendages to generate propulsive forces in GM (Figure 1D), 2) design of terradynamic control surfaces ("terrafoils") to counter the granular lift forces for ensuring continuous horizontal locomotion (Figure 1E), and 3) haptic detection of the position of obstacles around a moving body. Ultimately we implement these contributions into tethered and untethered robots capable of locomotion in GM. We have shown that the robot moves faster than any other untethered robot reported at a depth of 127 mm in a GM of density same as loosely packed sand.[30] We demonstrated that the robot can also function untethered in a challenging natural environment (at the beach), a feat that has not yet demonstrated by any other robot (Figure 1B and Movie S1, Supporting Information).

2. Results

This section includes details of the design of an untethered robot and results from the experimental tests for the characterization of individual appendages, the modulation of lift forces acting on the robot, the sensing of objects in GM, and the demonstrations of the robot in a natural environment and in the lab.

2.1. Design of an Untethered Appendage-Based Digging Robot

The robot was driven by two appendages through a sweep and propel motion as seen in animals.[31,32] To achieve a simple and robust actuation mechanism, we designed the appendages to be actuated by a single motor through a gearbox. The motor

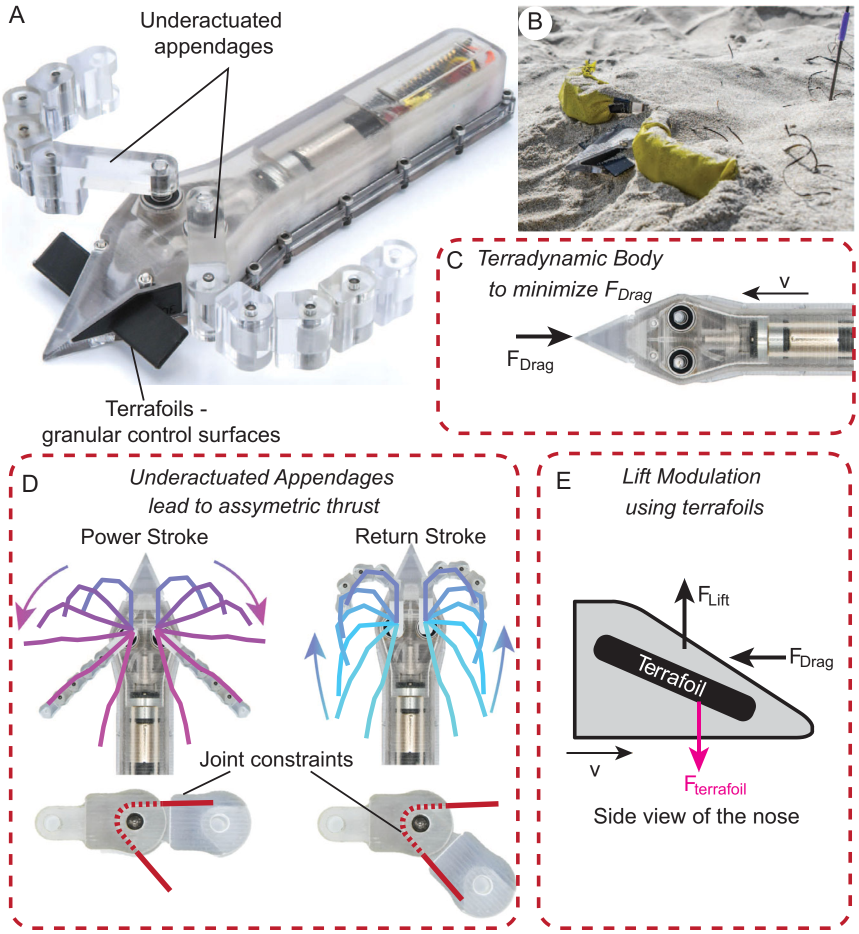

Figure 1. Overview of the robot. A) Photograph of the robot showing the underactuated appendages and terrafoils (granular control surfaces inspired by elevators and diving planes in airplanes and submarines respectively). B) Picture of the robot digging at a beach in San Diego. C) Top view of the optimized terradynamic body for minimizing the drag force in granular media. D) Time-series images showing the motion of underactuated appendages (created from tracked joint positions using the camera) in the power stroke and return stroke. The appendages were designed to experience minimum drag in return stroke and maximum propulsive force in power stroke for generating a net thrust to move forward. E) Side view of the sandfish lizard-inspired asymmetrically tapered nose with the terrafoils added to counter the lift force so that the robot stays submerged during locomotion.

position was controlled through encoder feedback and a proportional–integral–derivative (PID) controller. We selected a single motor for bilateral limb actuation to reduce the cross-sectional area of the body for reduced drag forces in GM (**Figure 2**A,B). The mechanical system that drove the appendages converted the rotation of the motor's output shaft, placed on the central axis of the robot, to rotation at the base of both appendages, using a worm drive transmission (Figure 2C).

The motor selection criteria were based on minimizing the cross-sectional area of the robot body while providing sufficient torque to drive the appendages. We used a DC motor with a planetary gearbox, as the stages of the gearbox stack axially, increasing the length and keeping the cross-section constant. The body was designed to have an *O*-ring and two water-tight bearings to ensure that it was sealed against both sand and water. The sealing was sufficient for movement in dry sand as studied here, and the robot was capable of operation without any signs of grains entering the body in all the experiments.

2.1.1. Design of the Robot Body

Forces within GM can be extremely high due to the weight of the sand and the friction forces between sand grains. Thus, to enable locomotion of a robot in GM, we needed to minimize the drag on the body of the robot. Our goal was to choose the body with the least projected area perpendicular to the direction of motion. To measure the drag force, we dragged bodies with four different profiles, but with constant frontal projected cross-section areas, at a constant velocity in a controlled granular environment (**Figure 3**A,B). We found that the body with a uniform cross section (shown in blue in Figure 3B) experienced the maximum drag force (F_D). The tapered body (green) with the same length L experienced a drag force of $\approx 15\%$ lower than the constant cross-section body (blue). Reducing the length of the body by 1/4 L, we found that the drag reduced by $\approx 7\%$, likely due to the reduced skin friction between the grains and the body. We finally tested a body with serrated edges (orange) but did

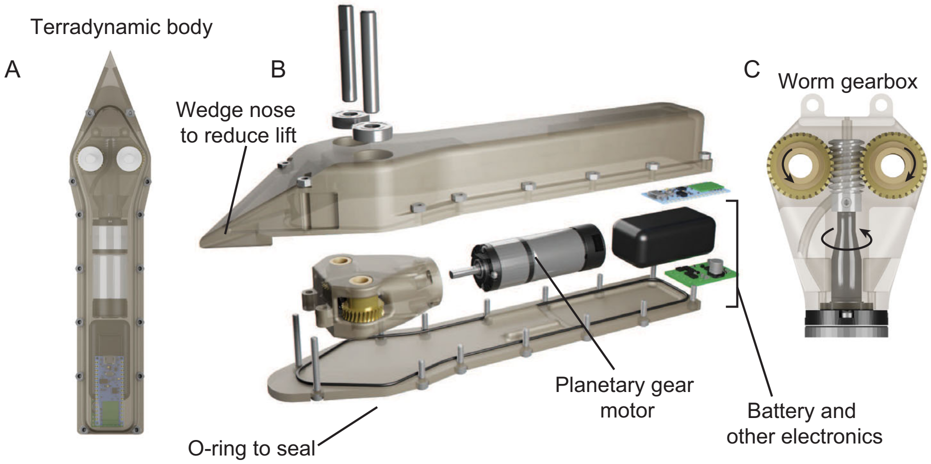

Figure 2. Robot design. A) Top view of the terradynamic body for the robot. B) Exploded view of the robot body assembly with different components. A planetary gear motor actuated both the appendages through a worm gear transmission. The robot was designed to be fully untethered with all the electronics encased in the body, fabricated using a resin 3D printer. An *O*-ring and two water-tight bearings were used to seal the body from sand and water. The appendages were driven by the motor through the two shafts attached to the gearbox. Wireless communication was done through a low-level messaging protocol (MQTT) through a wireless internet connection. C) A worm gear mechanism integrated into a 3D-printed gearbox allowed the robot to be actuated with a single motor.

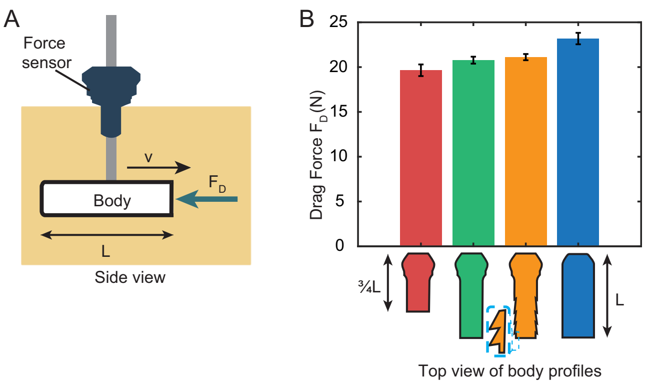

Figure 3. Drag tests for selecting the most terradynamic body. A) Schematic of the experimental setup used to measure drag on different body profiles. B) Experimental results for drag force acting on the four different test bodies. The drag force depends on the length of the body and body profile.

not find a considerable difference in force with the nonserrated tapered body (green) in both forward and backward directions. These experiments led us to choose the tapered body design instead of a solid body with a constant cross section. We also incorporated a shovel-shaped nose in front of the body to counter the upward lift forces acting on the body (Figure 2B).

2.2. Design and Characterization of the Appendage

After designing the robot body, we performed a series of tests to find the optimal curvature of the appendage for maximizing forward thrust on the robot. To contend with the large resistive forces in GM, we used rigid links machined from aluminum, with revolute joints constrained by joint angles. Each appendage consisted of five links actuated at the base. Each link had variable joint constraint angles at 15° increments enforced by pins inserted into 1 of 12 holes (**Figure** 4A).

2.2.1. Design of the Appendage for Maximizing Forward Thrust

First, we measured the torque τ at the base of an appendage undergoing an oscillatory motion to mimic the thrust and return strokes of our robot. We varied the angular amplitude of oscillatory motion ϕ in addition to the angular range β of the underactuated joints (Figure 4B). We also measured the steady-state torque for the appendage in bent and straight configurations for different joint angles by rotating the appendage by two full rotations in both directions. It was observed that for bent configuration (return stroke), torque decreased with the increase in the joint constraint angle β due to the decrease in drag (Figure S1B, Supporting Information).

Next we oscillated the appendage at a constant angular velocity; the reaction torque magnitude due to the drag of GM, τ, decreased during the power stroke because the links bent passively to stop at the upper joint constraint angle until the linkage became straight, leading to maximum drag (Figure 4C). The step decrease observed in the power stroke was likely due to each of the links reaching the upper constraint on the joint angle. During the return stroke, torque magnitude increased quickly because the linkage started to bend at the joint closest to the shaft followed by a slow increase to the maximum value when all the links reached their upper constraint angle β. The torque in all these experiments was negative for the power stroke and positive for the return stroke. We performed this experiment for β ranging from 15° to 90° in 15° intervals. The asymmetry in torque was measured as the net mean value of the torque in a cycle. This asymmetry is approximately proportional to the net propulsive thrust required to move forward.

We observed that for low amplitudes of oscillation ($\phi = 60°$ and 120°), the maximum torque of the power stroke (in the negative direction) didn't change much with the constraint angle β.

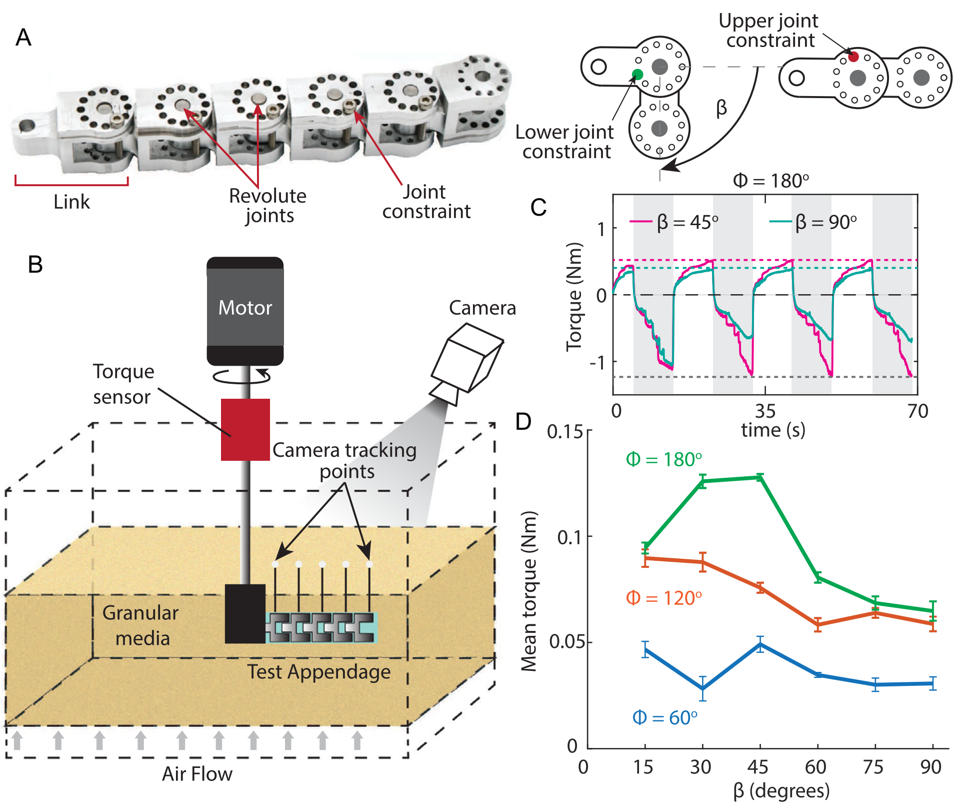

Figure 4. Design and characterization of underactuated appendages. A) Photograph of the computerized numerical control (CNC) machined linkage with five links and five joints with variable joint constraint angles at 15° increments enforced by pins inserted into one of 12 holes. The lower joint angle is denoted by β and the upper joint angle is fixed at 0°. B) Schematic of the experimental setup. C) The torque output for $\beta = 45°$ and 90° (mean of five trials) for amplitude of oscillation $\phi = 180°$. We observed asymmetry in torque between power and return strokes because of the asymmetric joint constraints. D) Net mean torque (mean of five trials for last cycle, error bars show standard deviation) for the peak amplitude of $\phi = 60°$, 120°, and 180° for different constraint angles β.

At low oscillation amplitudes, the links which start in a bent configuration (from the previous return stroke) are not able to open fully to their upper joint constraint and thus the joint constraint limit doesn't influence the net torque (Figure S1A, Supporting Information). However, for a large amplitude of oscillation ($\phi = 180°$), the joints are able to reach their upper angle constraint and we observed that this maximum torque decreased after the first cycle for $\beta > 45°$ (Figure 4C). This behavior was unexpected since the steady-state torque during the return stroke decreased with the increase in constraint angle β. From the torque data, it was evident that there was an optimum joint angle β for maximum asymmetry in torque, at this large amplitude of oscillation. We measured the net mean torque in a cycle for different β values and found that there existed an optimum value of mean torque at $\beta = 45°$ for the amplitude of oscillation $\phi = 180°$. For the angle $\beta > 45°$, the mean torque started decreasing until reaching the lowest value at $\beta = 90°$ (Figure 4D).

2.2.2. Suboptimal Configurations of the Appendage Leading to Reduced Performance

To understand the decrease in torque for $\beta > 45°$ at large amplitudes of oscillation, we calculated the joint positions at each time step from the tracking points using the data from the camera. We observed that for $\beta \leq 45°$, the linkage bent to reduce drag during the return stroke and reached the maximum drag configuration (straight) in the power stroke, as we anticipated (**Figure 5**B). However, for $\beta > 45°$, the linkage didn't reach the maximum drag configuration in the power stroke and got stuck in a collapsed configuration (Figure 5A). This behavior was prominent at higher joint angles (Figure 5C). We measured the shape of the linkage at the end of each power stroke for the last three cycles and observed that for $\beta \leq 45°$, the appendage was straight in the maximum drag configuration for all cycles (Figure 5D). However, for $\beta > 45°$, the shape of the linkage at the end of the power stroke remained collapsed in a bent configuration for all cycles.

To gain insight into what joint locking angles would result in a collapsed configuration, we calculated the net torque acting on the distal link for different uniform configurations (where all joint angles are at β; Figure 5E). The torque was calculated by numerically calculating the resistive forces from granular media that act on the end link using the method originally reported in ref. [3]. We calculated the RFT force perpendicular to the link along the length (sampled at 20 points from base of the link to end). From the perpendicular forces along the link, we computed the net moment acting at the joint, τ, which we plot in Figure 5E. We observe that for low locking angles, the net torque

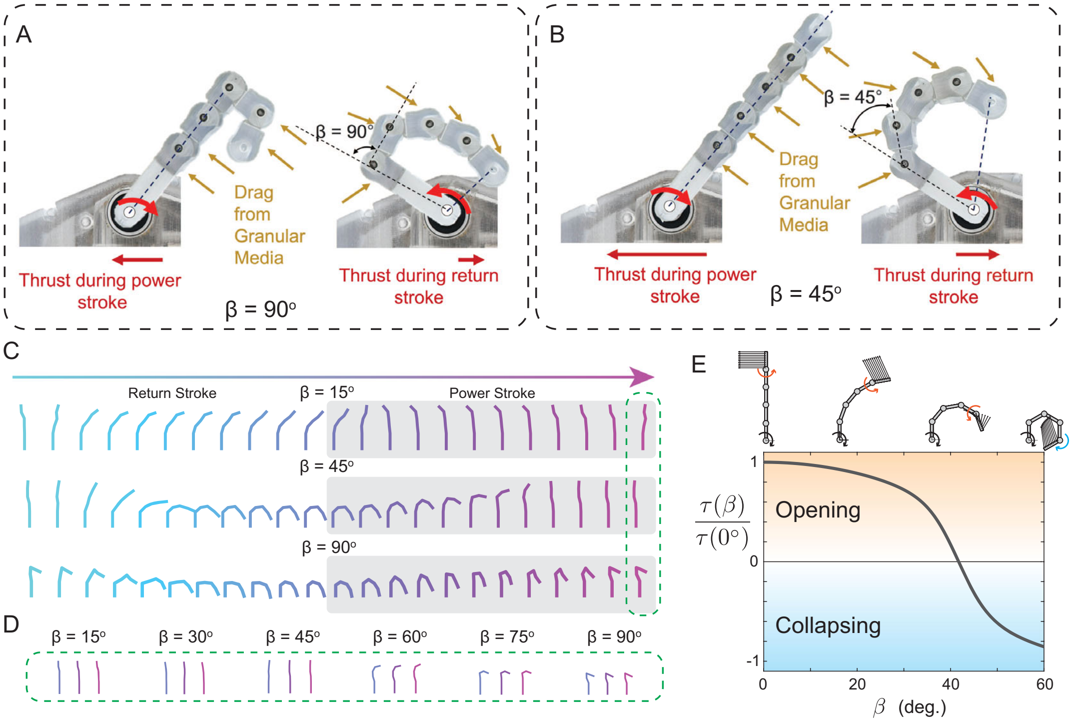

Figure 5. Visualization of appendage curvature. A,B) Schematics showing the effect of joint constraint angle $\beta = 90°$ and $\beta = 45°$ on the movement of the appendage respectively. In the case of $\beta = 45°$, the appendage opened up to reach the maximum constraints during the return stroke due to the drag of granular media; during the power stroke, the appendage pushed the grains to generate a net propulsive force for the robot to move forward. In the case of $\beta = 90°$, the appendage reaches maximum bent configuration in the return stroke. During the power stroke, the appendage was not able to fully straighten up which caused the links at the end to reach suboptimal configurations resulting in reduced net forward thrust. C) Time-series images of the linkage configuration seen in its rotating frame, as measured from the LED markers used for optical tracking (mean of five trials) for one period of $\phi = 180°$ oscillation. D) Tracked configurations of the linkage at the end of the power stroke for the last three cycles of oscillation for different constraint angles β, showing that once the linkage gets stuck in a bent configuration such as for $\beta = 90°$, it stays bent for multiple cycles. E) RFT calculation of net torque on end link in different bent configurations. As the locking angle is increased for homogeneous bent configurations (all angles equal to β, we observe that the net torque changes sign for increasing β. When β is small the net torque on the end link is positive due to a clockwise rotation of the base (black arrow in upper diagrams). Positive torque will cause the linkage to want to open up. As β increases the net torque decreases until at $\beta = 41.75°$ the torque changes sign, causing the linkage to collapse inwards.

on the end link during the power stroke is positive, causing this joint to open up to a straight configuration. However, as β increased, the RFT force resulted in a transition to a negative torque acting on the end link (at $\beta = 41.75°$), which would cause this link to collapse inwards. These results provide evidence that there is a tradeoff between allowing the appendage to collapse during the return stroke: for large locking angle, the appendage produces small drag during the return stroke because it collapses; however, when the locking angle is too large the limb gets stuck in a collapsed configuration because of the RFT forces acting on the end link.

We observed that even if the appendage oscillated at a very large amplitude of $\phi = 360°$, the end linkage still remained stuck in the collapsed configuration because external drag forces acted on the links in a direction opposite to the direction of velocity forcing the last links to remain stuck. These results informed us that once the appendage is deformed in a suboptimal configuration such as for $\beta = 90°$, it will stay in that configuration for subsequent cycles too (Figure S2, Supporting Information). Thus, we concluded that we should choose an appendage with joint constraint angle near the regime where the end-link torque, τ, causes collapse. We chose a locking angle of $\beta = 45°$ as it was near the RFT-predicted collapse locking angle, and in experiment always was able to collapse during the return stroke, and open fully during power stroke.

2.3. Modulation of Lift Forces

We tested the robot with the appendages selected from the previous section study and found that the robot repeatedly would rise to the surface, as has been observed in other digging robots.[33] In prior work, it has been demonstrated that the angled design of head shape[33] or adding control surfaces[34] can cause robots to counter lift forces in granular media. To keep our robot at a level depth, we designed control surfaces called “terrafoils” (granular force control surfaces) to the side of the nose to control lift similar to how elevators in airplanes and diving planes in submarines are used to control pitch. The goal of these surfaces was to counter the upward lift force acting on the body without increasing the resistive drag. We measured drag and lift forces acting on terrafoils of varied geometry to minimize drag F_D and

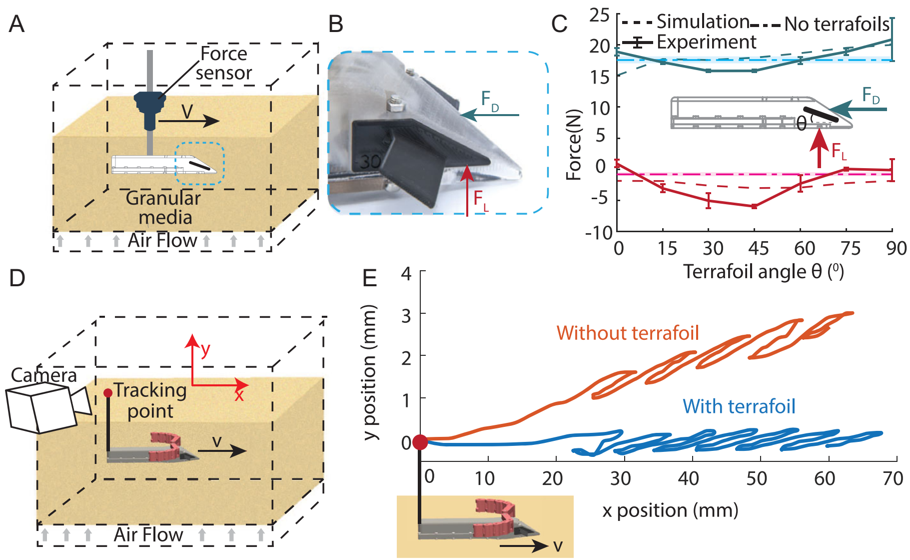

Figure 6. Modulation of lift forces using terrafoils. A) Experimental setup for measuring drag and lift on the robot with terrafoils of different angles θ. B) The nose of the robot with terrafoils attached to the side. C) Experimental (solid lines) and simulation (dashed lines) results for drag and lift forces for terrafoils of different angles and aspect ratio = 1. The body drag and lift without terrafoils is shown in cyan and pink with the shaded region showing the error bar for the mean value of five different trials. The terrafoil with $\theta = 15°$ performed the best as it had the minimum drag and the maximum downward lift. D) Schematic describing the free-swimming tests where the robot swims in the sand with a tracking marker with and without terrafoils E) The trajectory of the robot is measured by the position of the marker in x and y directions for the robot with and without terrafoils for $\theta = 30°$. y displacement stayed constant for the case when terrafoils were attached to the nose without much decrease in the speed in the x-direction. The first stroke is longer than the others because we start the robot in power stroke with appendages fully extended (maximum drag).

maximize downward lift force F_L (**Figure 6**A,B). We tested terrafoils at different aspect ratios at an angle $\theta = 15°$ from the horizontal but having the same frontal area of projection A. According to RFT for terradynamics,[10] the drag F_D and lift F_D forces on an intruder are directly proportional to the projected frontal area of a cross section if the depth and the orientation remain the same.[10] However, we found that a unity aspect ratio experienced the least horizontal drag and maximum downward lift (Figure S4, Supporting Information).

Next, we tested the terrafoils at different angles θ to find the optimum terrafoil with the maximum negative F_L with the least F_D in GM. We observed that the horizontal drag (F_D) experienced by the body with terrafoils attached first decreased and then increased, with the angle θ as the projected area of cross-section increased (Figure 6D). We believe that the drag force experienced by the body with terrafoils decreased because the terrafoils were added at the nose just in front of the widest cross section of the body (where the gearbox fits; Figure 2C), which may have caused the grains to flow before they interact with the body, reducing the net drag. Additionally, the net projected surface area of the terrafoils was much less than the area of the cross section of the body, which may help explain why we did not see much difference in the drag as compared to the body with no terrafoils. However, we noticed that the terrafoils changed the lift force significantly as we saw a clear trend where the lift forces F_L decreased with θ from 0° to 45° and then increased with θ from 45° to 90°. The negative lift force in all these experiments indicated a downward force acting on the robot. We also performed modeling for these trends using a modified version of RFT (Modeling Methods section of Supplementary Materials) and found that the results matched very well with the experiments (Figure 6C). In future work, it will be beneficial to incorporate 3D RFT[35–38] and discrete element method (DEM) simulations to optimize the location of terrafoils and their effect on granular lift on the robot.

To demonstrate the application of terrafoils on the robot propelled by the asymmetric action of the appendages (Figure 6E), we tracked the position of the robot using a tracker on a rod sticking out of the GM. We observed that the robot had an upward y displacement of 3.41 for 70 mm of horizontal displacement in 37 s (speed of 1.20 mm s^{-1} with fit with 95% confidence bounds) (Figure 6E). Next we added the 30° terrafoils on both sides at the front of the robot to produce a net moment about the center of pressure that rotates the robot head downward while moving horizontally in granular media. This location was chosen to make sure that the body doesn't rotate upward while moving horizontally in GM (Figure 6B). We ran the experiment again and found that the robot stayed oscillating around the 0 mm y displacement for 61.27 mm of x displacement in 37 s (speed of 1.03 mm s^{-1} with 95% confidence bounds)(Figure 6E). These results demonstrated that granular lift force can be modulated by adding terrafoils to enable a robot to swim horizontally in GM without surfacing.

2.4. Sensing Obstacles in Granular Media

A potential advantage of appendage-driven locomotion in GM is the detection of obstacles away from the body by measuring the

ADVANCED INTELLIGENT SYSTEMS Open Access
www.advintellsyst.com

appendage resistance force during swimming. We performed systematic benchtop experiments to understand how the presence of obstacles around an oscillating rigid plate affects the grain flow and thus the force exerted on a rigid rotating fin (we used a fin 3D printed out of acrylonitrile butadiene styrene [ABS]). The obstacle chosen for experiments was a flat plate that was placed at different orientations and distances with respect to the rotation axis of the appendage. When the plate was placed above and parallel with the appendage sweep plane, there was a peak in the torque (indicating the presence of obstacle) acting at the shaft attached to the fin (Figure S6 and S7, Supporting Information). We calculated the difference between the max torque when the obstacle was near and when it was far. We found that the torque difference value was remarkably high (≈ 0.5 Nm) when the flat plate obstacle was above and parallel with the appendage sweep plane (**Figure** 7B). We saw a similar, but lower magnitude, change in the torque when a vertical plate was above the fin. However, there was not an appreciable change in torque for the cases when the obstacle plate was in front of the fin and when the obstacle was below the fin. This can be explained by the flow of grains moving upward in granular media[39] and not getting disturbed by the presence of an obstacle below the moving fin. The depth-dependent forces in granular media, in combination with friction between grains, results in an upward flow of GM in response to the translation of an intruder[25,40] and thus it is likely only obstacles that disrupt this flow will cause a change in force. Thus, our experiments indicate that a robot with oscillating appendages may be able to detect obstacles over it but not under it. It could also not detect obstacles parallel to the direction of motion (wall obstacle).

To demonstrate sensing on the robot, we added a force sensor at the last link of one of the appendages (Figure 7C). As the robot moved under the obstacle placed 10 mm above it (Figure 7F), we measured the force sensor voltage through a data

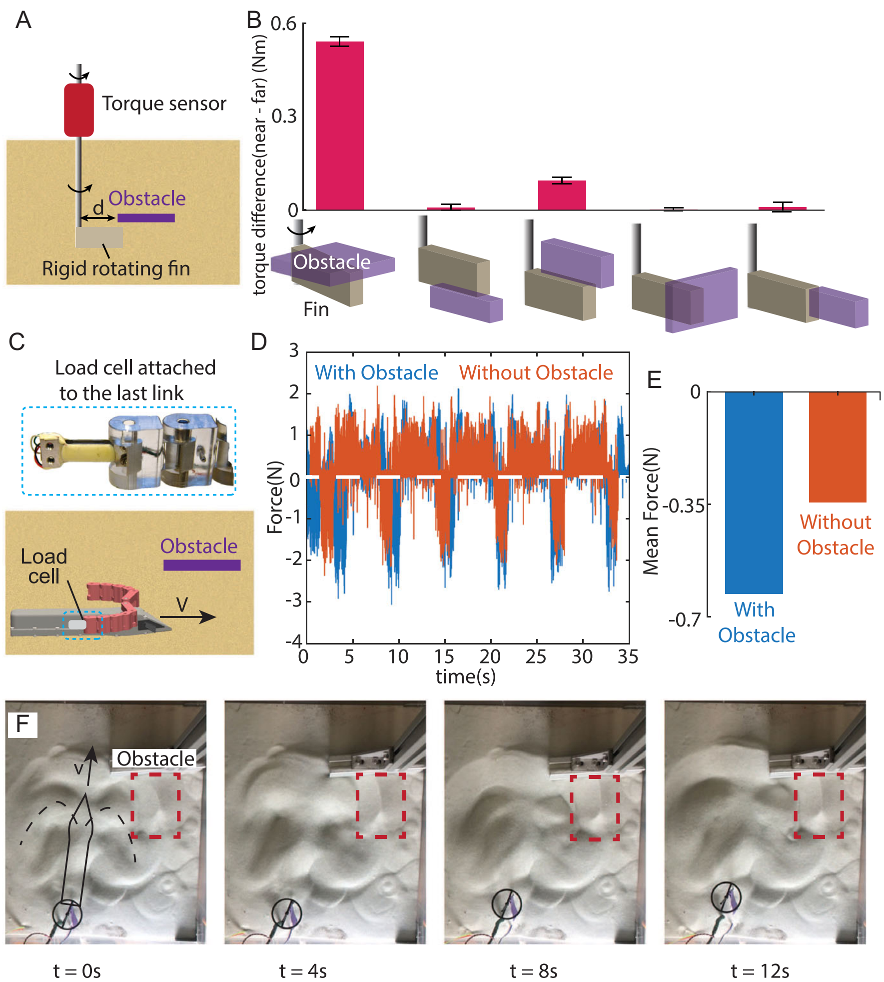

Figure 7. Obstacle detection from differential grain resistance. A) Schematic of the sensing experiment to understand the effect of an obstacle on a rotating fin. B) Difference of torque between the cases when the obstacle was far and when it was near for five different configurations. C) Schematic of the robot moving under the obstacle with inset showing the location of the load cell. D) Raw data from the force sensor for the two cases of with and without obstacle. E) Mean of the force measured from the force sensor was more when the robot moved under an obstacle than when the robot moved without an obstacle. F) Time-series snapshots of the top view of the robot moving under the obstacle (Movie S1, Supporting Information).

acquisition system (DAQ). We found that in one cycle of appendage motion, the force was positive during the return stroke and some part of the power stroke until the appendages opened up to exert force in the other direction (Figure 7D). We found that the net mean force measured from the force sensor in the case of the robot moving under the obstacle was more than when there was no obstacle (Figure 7E). This validated and demonstrated our results from systematic sensing experiments as we could detect the obstacle above the robot as it moved under it.

2.5. Performance of the Robot in the Wild and in the Lab

We tested the robot in the fluidized sand bed at a depth of 127 mm from the top. For every test run, we placed the robot horizontally inside the GM using the fluidization of the bed and observed the disk marker attached to the carbon fiber tracking rod. We found that in the lab experiments the robot speed varied from 1.2 to 1.6 mm s^{-1} (Movie S1, and S2, Supporting Information, **Figure 8**B). These tests were performed both tethered for maximum current and untethered on a fully charged battery and both showed similar performance in the controlled granular bed.

We also tested the robot in a natural environment (at Scripps Beach, La Jolla, CA, US). Since the robot was not designed to be able to self-burrow, we performed experiments by placing the robot at a depth of 127 mm (Figure 8A) (observed through the carbon fiber marker) and distributing sand over the top. We initiated the experiments with wireless control. We observed that the robot was able to move forward in the natural sand for a distance of $\approx$ 30mm at a speed of 0.57 mm s^{-1}. We believe that the decrease in the speed of the robot relative to lab experiments in controlled glass beads was due to several factors. 1) It has been shown previously that natural sand is harder to dig in than dry glass beads due to the irregular shape of the sand grains,[10] 2) the sand at the beach had other debris intermixed such as seaweed (Movie S1, Supporting Information) which may have reduced its ability to flow,[41] and 3) the sand at the beach had a higher moisture content than the glass bead used in the lab; after digging the hole for the robot, we observed that the sand at the depth of 127 mm was wet. Wet sand presents significantly larger resistive forces for intruders when the moisture range is in between completely dry and completely saturated,[42] which causes the motor to stall.

3. Discussion

The objective of this study was to demonstrate the application of underactuated appendages with different bending angles, due to asymmetries from joint angle constraints, to generate thrust while interacting with the granular media. This underactuated appendage was controlled using a single motor connected to a worm drive which enabled the design of the robot to be compact and lightweight as compared to previous approaches.[13] Previous work has demonstrated a compliant fin-based robot for locomotion in granular media, where the actuation parameters were optimized while the limb compliance was held constant.[23] The design strategy of generating asymmetric thrust presented in this work is very robust and versatile as compared to designing specifically for a particular granular material since the optimum joint angle constraints are independent of depth, the size and shape of the grains, and the packing fraction of GM. This can also inform the understanding of how the geometry and compliance of animal appendages, such as turtles' flippers,[43,44] generate a positive thrust in GM.

This work may offer insight into the design of other robots with underactuated linkages for locomotion in GM. For example, the locomotion of snake-like robots with passive elastic joints has been studied in viscous fluids[45] and the role of flexible appendages has been studied in robophysical models of quadriflagellate bacteria.[46] However, in GM, the nonzero yield stress presents the opportunity for robot links to become locked in suboptimal configurations. Underactuation is likely an important design consideration for locomotion in GM since the torque requirements at joints can be very large. We found the optimum joint angle for the appendage considering a uniform curvature for simplicity, that is, all the links have the same joint constraint; however, it is possible that the optimum constraint varies along the length of the appendage and each link has a different optimum. Future work could address these questions, taking a larger set of link geometry parameters using numerical methods such as the DEM.

The forward speed of the robot was $\approx$1.2 mm s^{-1} when at a depth of 127 mm. This may seem quite slow for robot locomotion; however, granular material presents significant challenges from the depth-dependent forces and friction. The speed of this robot is consistent with other bioinspired burial robots (e.g., see Table 2 of Ref. [30]). From our experiments we anticipate that there are several possible methods to increase the robot speed. The first method is to increase the gait cycle frequency. Since the

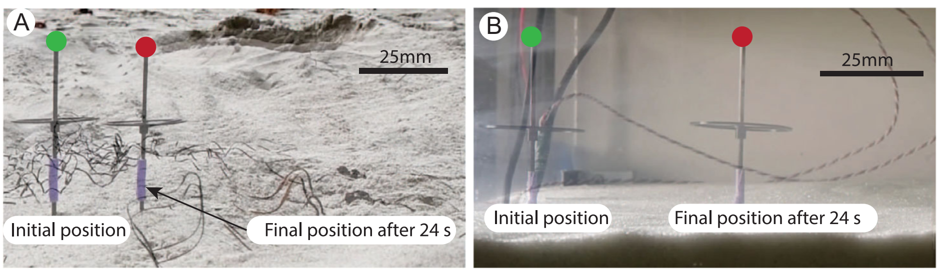

Figure 8. Robot demonstration at the beach and the lab. A) Initial and final positions of the robot at a demonstration at the beach at a depth of 12.7 cm. The robot moved at a speed of 0.57 mm s^{-1}. B) Initial and final positions of the robot moving in the controlled granular environment (glass beads) with a packing fraction of $\approx$ 0.58 (loosely packed) at the same depth with a speed of 1.2 mm s^{-1}.

granular forces do not depend on speed in the noninertial regime,[47,48] speed of the robot should linearly vary with gate cycle frequency. A second method for increasing speed would be to make the appendages longer so that during each stroke the robot moved forward a longer percentage of its body length. Both of these methods come at the expense of requiring higher power actuation and it is unknown how the overall cost of transport may vary across these design choices. This will be interesting work for future experiments.

Our experimental results indicate that a smoothly tapered "terradynamic" body is better than having a body with a constant area of the cross section with the same projected frontal area, which can be tested using numerical approaches for future work. Although other research groups have shown the benefit of a tapered nose[33] and of adding a wedge-shaped foil to reduce lift,[49] our approach was to study the effect of the geometry of these modular control surfaces and to experimentally verify the reduction of lift forces without increasing horizontal drag by adding "terrafoils". According to granular RFT,[3,10] the terrafoils with a similar area and different aspect ratios should have the same drag and lift, which is different than what we found. These experimental results generate an understanding of how drag and lift forces can be changed by adding modular control surfaces for digging robots in the future. Future work can also explore making actuated terrafoils on the front and the back of the robot to control the pitch of the robot while swimming in the sand, similar to diving planes in submarines.

In general, our experimental study indicates that by measuring the differential granular resistance around a moving body, an obstacle above the body can be detected but not below the body. This result suggests how GM behaves completely different than fluids, where a symmetrical rigid rotating plate will have a symmetric flow of fluid above and below the plate. Future work could use the studies presented here to explore haptic identification and modeling of objects in granular media. To further show the benefit of having an appendage-based locomotion mechanism, we have shown how the appendages can be used to sense objects in the sand away from the body by sensing the granular flow, a strategy employed by many arthropods.[50] Future work can explore the detection of objects on either side of the robot by measuring the force difference between the two force sensors. Sensing can also be used to detect if the robot is trying to pitch upward/rise toward the surface or pitch downward/swim toward the bottom by measuring the force from both the appendages as the drag force increases linearly with depth.

The experiments performed in this work led to the design of a two appendage-driven robot with symmetric actuation during the power and return strokes. This robot can be deployed in the wild because of its small form factor (can be easily held in a hand) and being fully untethered. This robot has the potential for steering by controlling the bend and locking angles on the appendages. The asymmetry in the forces between left and right appendages will cause the robot to steer. The robot body made for this work was designed to be watertight and future work can explore testing in fully submerged granular media such as granular ocean surface, where the fully saturated grains behave similarly to dry granular media except with lesser particle–particle friction.[42,51] We believe that we would see a similar performance for this robot in submerged sand as the slow movements of the appendages will likely not change the resistive forces from the GM. Further, along with swimming in grains, appendages can be used for swimming in the water by changing the robot body to have negative buoyancy elements so it does not sink and changing the actuation parameters for faster strokes. Future appendage-enabled robots can be designed to be deployed from the ocean surface to swim in the water and transition from water to submerged sand to navigate the seabed.

Currently, there are some practical challenges to deploy the robot in the wild because it cannot perform self-burrowing from the surface. However by manipulating limb motion such as in the sandfish lizard,[52,53] this robot can be designed to penetrate into and come out of granular media. Improvements can also be made for self-burrowing by either adding two more appendages such that there is a pair at top and bottom of the body for belly-first transitions such as in sand vipers,[54] or using actuated terrafoils to fluidize the sand in the front, or a combination of both to enable head-first transitions similar to wrassefish.[55]

In the current body design, a single battery (450 mAh) charge can enable this robot to run for ≈ 5 min with a net distance traveled of ≈ 30cm (assuming a speed of $1\,\mathrm{mm\,s^{-1}}$ at 127 mm depth). However, as our body shape experiments demonstrate, there is only a small increase in body force as the robot body is elongated. Thus we envision future robots will have longer bodies for larger motors and batteries with multiple appendages.

Applications of this robot include deploying on extraterrestrial bodies with granular media such as the sandy surfaces of Mars[56,57] and asteroids.[1,58] This robot can be modified to deploy in submerged sand and can be used for sensing and monitoring the submerged sand bed in the ocean and for self-anchoring of ships. This robot also has applications in agriculture and soil studies where it can be used for contaminant monitoring of the soil. Another application for this robot can be measuring moisture content in grain silos as a moisture sensor can be easily integrated on the robot appendage and can also be used in search and rescue operations during grain entrapment in these silos.

4. Experimental Section

Fluidized Granular Bed: In all the lab experiments, we used an air fluidized bed of cross section 43 by 43 cm which was filled with dry spherical glass beads of diameter $212-300\,\mu\mathrm{m}$ (Potters Industries with density $\rho = 2.51\,\mathrm{g\,cm^{-3}}$) to a depth of 17.78 cm. No moisture was added to the granular material and thus these are considered "dry" granular material consistent with other locomotion-based experiments.[3,39] The base of the testing platform was made of a porous plastic membrane with a pore size smaller than the grain diameter. The porous floor was supported by an aluminum honeycomb structure with an empty volume underneath to install the outflow of a commercial shop vacuum (6.5 HP). The shop vacuum was connected to the AC power source through a proportional relay controlled by an analog output signal through a Data Acquisition Card (National Instruments). The flow rate for air going through the GM was controlled by varying the analog output voltage. The volume fraction ϕ was calculated by taking images of the bed height h and substituting other values in the equation $\phi = M/\rho A h$ where M, A, and h are the total mass of the grains, area of the bed, and height of the bed respectively.[25] Before every trial, airflow through the porous membrane fluidized the medium[20] and then we ramped down the flow rate slowly to get our desired packing fraction ϕ measured as 0.58 ± 0.03, which falls in the range of loosely packed sand found in natural environments.[59]

Materials used in the Design of the Robot: Considering the planetary gear motor's stall torque of $\approx$1.13 Nm (116 rpm, Actobotics), a worm drive with a gear reduction of 15:1 was chosen, resulting in a net max torque of 16.95 Nm which was more than enough to move the two appendages. The battery used in the untethered robot was decided based on the dimensions and the discharge rate. The battery had a capacity of 450 mAh with a discharge rate of 45 C (Turnigy Nano-Tech 450 mAh) which was sufficient to provide the maximum current to the motor. The body and the gearbox was fabricated using a resin 3D printer (Objet 350 Connex 3, Stratasys Inc.; Material:Veroclear). This printer material was chosen for accuracy, strength, fast prototyping, being water and sand tight as well as easy removal of soluble support material. The drag experiments on the body informed the use of tapered body. Inspired by previous studies of the sandfish lizard,[3,60] we designed the body with an asymmetrically tapering wedge-shaped nose, inclined at an angle of 30° to reduce the lift forces acting on the body.

We printed the links for the robot appendages on the same 3D printer and each link had the optimum joint constraint angle $\beta = 45°$. We chose the area of cross section of the appendage links such that the effective area of cross section of the appendage is always greater than the area of cross section of the body. In other words, the propulsive force generated by the appendages was always greater than the drag force experienced by the robot. Another parameter that limited the propulsive force produced by the appendages was the motor torque as a larger appendage link would have generated more propulsion but it would have come at a cost of increasing motor size which in turn would have increased the robot cross section area, thereby increasing drag.

The untethered robot had a length of 25.6 cm, width of 5.1 cm (widest part), and a height of 3.2 cm. To enclose the appendages from sand, we sewed a pouch using silicone-coated fabric (Ripstop Nylon, Seattle Fabrics) and a silicone adhesive (Silnet Seam Sealer, Gear Aid) was used to seal the seams. The optimum angular sweep of the robot appendages was selected to be $\approx 160°$ $(90° + 70°)$ such that the appendages reached maximum angle while return stroke (parallel to the body) was able to straighten near the farthest point of the body to generate maximum propulsive force (Movie S1, Supporting Information).

Please refer to the *Experimental* Section of Supplementary Material for more details on the experiments.

Supporting Information

Supporting Information is available from the Wiley Online Library or from the author.

Acknowledgements

The authors would like to thank Qifan Yufor rendering the robot body assembly, Caitlin Le for helping in the beach tests, Iman Adibnazari for help with MQTT protocol, and all the members of Gravish Lab and Bioinspired Design and Robotics Lab for general assistance. The authors would also like to thank Thomas Chalfant and Ian Richardson from MAE Machine Shop for help in fabricating components. This material is based upon work supported by the Office of Naval Research under grant number N00014-20-1-2373. Any opinions, findings, and conclusions or recommendations expressed in this material are those of the author(s) and do not necessarily reflect the views of the ONR.

Conflict of Interest

The authors declare no conflict of interest.

Author Contributions

S.C. performed the experiments, designed the robot, and wrote the manuscript. D.V. designed and fabricated the robot and performed experiments. S.J. performed modeling and wrote the manuscript. M.T.T and N.G. advised on designing the robot, conducting experiments, and writing the paper.

Data Availability Statement

The data that support the findings of this study are available in the supplementary material of this article.

Keywords

appendage, digging, granular media, robot, sensing, underactuated

Received: November 19, 2022
Revised: March 15, 2023
Published online:

[1] H. Miyamoto, H. Yano, D. J. Scheeres, S. Abe, O. Barnouin-Jha, A. F. Cheng, H. Demura, R. W. Gaskell, N. Hirata, M. Ishiguro, T. Michikami, A. M. Nakamura, R. Nakamura, J. Saito, S. Sasaki, *Science* **2007**, *316*, 1011.
[2] A. Hosoi, D. I. Goldman, *Annu. Rev. Fluid Mech.* **2015**, *47*, 431.
[3] R. D. Maladen, Y. Ding, C. Li, D. I. Goldman, *Science* **2009**, *325*, 314.
[4] C. Li, K. Lewis, *Adv. Intell. Syst.* **2022**, *5*, 2100195.
[5] A. Martinez, J. DeJong, I. Akin, A. Aleali, C. Arson, J. Atkinson, P. Bandini, T. Baser, R. Borela, R. Boulanger, et al., *Géotechnique* **2021**, 1.
[6] D. Ortiz, N. Gravish, M. T. Tolley, *IEEE Robot. Automat. Lett.* **2019**, *4*, 2630.
[7] K. Isaka, K. Tsumura, T. Watanabe, W. Toyama, M. Sugesawa, Y. Yamada, H. Yoshida, T. Nakamura, *IEEE Access* **2019**, *7* 103127.
[8] B. Liu, Y. Ozkan-Aydin, D. I. Goldman, F. L. Hammond, in *2nd IEEE Int. Conf. on Soft Robotics (RoboSoft)*, IEEE, Piscataway, NJ, **2019** pp. 828–833.
[9] A. A. Calderón, J. C. Ugalde, J. C. Zagal, N. O. Pérez-Arancibia, in *IEEE Int. Conf. on Robotics and Biomimetics (ROBIO)*, IEEE, Piscataway, NJ **2016**, pp. 31–38.
[10] C. Li, T. Zhang, D. I. Goldman, *Science* **2013**, *339*, 1408.
[11] T. Zhang, D. I. Goldman, *Phys. Fluids* **2014**, *26*, 101308.
[12] J. Gray, G. Hancock, *J. Exp. Biol.* **1955**, *32*, 802.
[13] R. D. Maladen, Y. Ding, P. B. Umbanhowar, D. I. Goldman, *Int. J. Robot. Res.* **2010**, *30*, 793.
[14] A. Sadeghi, A. Tonazzini, L. Popova, B. Mazzolai, in *IEEE Int. Conf. on Robotics and Automation*. IEEE, Piscataway, NJ, **2013**, pp. 3457–3462.
[15] N. D. Naclerio, C. M. Hubicki, Y. O. Aydin, D. I. Goldman, E. W. Hawkes, In *IEEE Int. Conf. on Intelligent Robots and Systems*. IEEE, Piscataway, NJ **2018** pp. 5918–5923.
[16] A. Sadeghi, A. Mondini, B. Mazzolai, *Soft Robot.* **2017**, *4*, 211.
[17] A. Thoesen, T. McBryan, H. Marvi, *RSC Adv.* **2019**, *9*, 12572.
[18] N. T. Jafferis, E. F. Helbling, M. Karpelson, R. J. Wood, *Nature* **2019**, *570*, 491.
[19] S. Kuindersma, R. Deits, M. Fallon, A. Valenzuela, H. Dai, F. Permenter, T. Koolen, P. Marion, R. Tedrake, *Autonom. Robots* **2016**, *40*, 429.
[20] C. Li, P. B. Umbanhowar, H. Komsuoglu, D. E. Koditschek, D. I. Goldman, *Proc. Natl. Acad. Sci. USA* **2009**, *106*, 3029.

[21] G. Bledt, M. J. Powell, B. Katz, J. Di Carlo, P. M. Wensing, S. Kim, *IEEE Int. Conf. Intell. Robots Syst.* ***2018***, 2245.
[22] Y. Chen, H. Wang, E. F. Helbling, N. T. Jafferis, R. Zufferey, A. Ong, K. Ma, N. Gravish, P. Chirarattananon, M. Kovac, R. J. Wood, *Sci. Robot.* **2017**, *2*, eaao5619.
[23] D. Li, S. Huang, Y. Tang, H. Marvi, J. Tao, D. M. Aukes, *IEEE Robot. Autom. Lett.* **2021**, *6*, 5984.
[24] R. A. Russell, *Adv. Robot.* **2011**, *25*, 119.
[25] N. Gravish, P. B. Umbanhowar, D. I. Goldman, *Phys. Rev. E Stat. Nonlin. Soft Matter Phys.* **2014**, *89*, 42202.
[26] H. M. Jaeger, S. R. Nagel, R. P. Behringer, *Rev. Mod. Phys.* **1996**, *68*, 1259.
[27] R. Patel, R. Ouyang, B. Romero, E. Adelson, *Spr. Proc. Adv. Robot.* **2021**, *19*, 105.
[28] S. Jia, V. J. Santos, in *Proc. of the RSS Workshop Tactile Sensing for Manipulation: Hardware, Modeling, and Learning*, Vol *15*, **2017**.
[29] S. Jia, L. Zhang, V. J. Santos, *IEEE Robot. Autom. Lett.* **2022**, *7*, 9953.
[30] H. Wei, Y. Zhang, T. Zhang, Y. Guan, K. Xu, X. Ding, Y. Pang, *Space Sci. Rev.* **2021**, *217* 1.
[31] Y. Zhang, J. Cao, Q. Wang, P. Wang, Y. Zhu, J. Zhang, *J. Bionic Eng.* **2019**, *16*, 319.
[32] (Eds: M. W. Hamrick, B. K. Hall), *Fins Into Limbs: Evolution, Development, and Transformation*, Vol *14*, **2007**.
[33] R. D. Maladen, P. B. Umbanhowar, Y. Ding, A. Masse, D. I. Goldman, in *Proc. – IEEE Int. Conf. on Robotics and Automation*, IEEE, Piscataway, NJ **2011** pp. 1398–1403.
[34] D. Drotman, S. Chopra, N. Gravish, M. T. Tolley, in *2022 IEEE 5th Int. Conf. on Soft Robotics (RoboSoft)*. IEEE, Piscataway, NJ **2022** pp. 261–266.
[35] S. Agarwal, A. Karsai, D. I. Goldman, K. Kamrin, *Soft Matter* **2021**, *17*, 7196.
[36] S. Agarwal, A. Karsai, D. I. Goldman, K. Kamrin, *Sci. Adv.* **2021**, *7*, eabe0631.
[37] S. Agarwal, D. I. Goldman, K. Kamrin, *Proc. Natl. Acad. Sci. USA* **2023**, *120*, 2214017120.
[38] L. K. Treers, C. Cao, H. S. Stuart, *IEEE Robot. Autom. Lett.* **2021**, *6*, 1887.
[39] Y. Ding, N. Gravish, D. I. Goldman, *Phys. Rev. Lett.* **2011**, *106*, 28001.
[40] N. Gravish, P. B. Umbanhowar, D. I. Goldman, *Phys. Rev. Lett.* **2010**, *105*, 128301.
[41] J. Sigren, J. Figlus, A. R. Armitage, *Shore Beach* **2014**, *82*, 5.
[42] N. Mitarai, F. Nori, *Adv. Phys.* **2006**, *55*, 1.
[43] N. Mazouchova, P. B. Umbanhowar, D. I. Goldman, *Bioinspir. Biomimet.* **2013**, *8* 26007.
[44] J. A. Fujii, D. McLeish, A. J. Brooks, J. Gaskell, K. S. Van Houtan, *PeerJ* **2018**, *2018*, 1.
[45] S. Ramasamy, R. L. Hatton, *Phys Rev E* **2021**, *103*, 032605.
[46] K. Diaz, T. L. Robinson, Y. Ozkan Aydin, E. Aydin, D. I. Goldman, K. Y. Wan, *bioRxiv* **2021**, 2021.03.14.434582.
[47] D. Chehata, R. Zenit, C. R. Wassgren, *Phys. Fluids* **2003**, *15*, 1622.
[48] K. Wieghardt, *Annu. Rev. Fluid Mech.* **1975**, *7*, 89.
[49] N. D. Naclerio, A. Karsai, M. Murray-Cooper, Y. Ozkan-Aydin, E. Aydin, D. I. Goldman, E. W. Hawkes, *Sci. Robot* **2021**, *6* 2922.
[50] J. Jér, J. Casas, O. Dangles, *Annu. Rev. Entomol.* **2010**, *55*, 505.
[51] J. Koivisto, M. Korhonen, M. Alava, C. P. Ortiz, D. J. Durian, A. Puisto, *Soft Matter* **2017**, *13*, 7657.
[52] H. C. Astley, J. R. Mendelson, J. Dai, C. Gong, B. Chong, J. M. Rieser, P. E. Schiebel, S. S. Sharpe, R. L. Hatton, H. Choset, D. I. Goldman, *J. Exp. Biol.* **2020**, *223*, jeb103564.
[53] S. S. Sharpe, *Ph.D. Thesis*, Georgia Institute of Technology, **2013**.
[54] B. A. Young, M. Morain, *Copeia* **2003**, *2003*, 131.
[55] T.-A. M. Tatom-Naecker, M. W. Westneat, *J. Fish Biol.* **2018**, *93*, 860.
[56] T. Shinbrot, N.-H. Duong, L. Kwan, M. M. Alvarez, *Proc. Natl. Acad. Sci. USA* **2004**, *101*, 8542.
[57] M. P. Almeida, E. J. R. Parteli, J. S. Andrade, H. J. Herrmann, *Proc. Natl. Acad. Sci. USA* **2008**, *105*, 6222.
[58] E. Asphaug, *Science* **2007**, *316*, 993.
[59] W. W. Dickinson, J. D. Ward, *J. Sediment. Res. A: Sediment. Petrol. Process.* **1994**, *64 A*, 226.
[60] R. D. Maladen, Y. Ding, P. B. Umbanhowar, A. Kamor, D. I. Goldman, *J. R. Soc. Interface* **2011**, *8*, 1332.

